Acta Pharmaceutica Sinica B 2026;16(1):458−469

Chinese Pharmaceutical Association
Institute of Materia Medica, Chinese Academy of Medical Sciences

Acta Pharmaceutica Sinica B

www.elsevier.com/locate/apsb
www.sciencedirect.com

ORIGINAL ARTICLE

Oxygen-boosted dual-section microneedle patch for enhanced drug penetration and improved photodynamic and anti-inflammatory therapy in psoriasis

Yaqi Yuan[a,†], Peng Jiang[a,†], Chuan Xiao[d,†], Jiapeng Lei[a], Bo Cheng[a,*], Hankun Hu[c,*], Wei Li[a,b,e,*]

[a]*Department of Stomatology, Zhongnan Hospital of Wuhan University, School of Pharmaceutical Sciences, Wuhan University, Wuhan 430071, China*
[b]*Taikang Center for Life and Medical Sciences, Wuhan University, Wuhan 430071, China*
[c]*Department of Pharmacy, Zhongnan Hospital of Wuhan University, School of Pharmaceutical Sciences, Wuhan University, Wuhan 430071, China*
[d]*Department of Microbiology, College of Basic Medical Sciences, Army Medical University, Key Laboratory of Microbial Engineering Under the Educational Committee in Chongqing, Chongqing 400038, China*
[e]*Hubei Provincial Key Laboratory of Developmentally Originated Disease, Wuhan 430071, China*

Received 13 April 2025; received in revised form 25 June 2025; accepted 18 July 2025

KEY WORDS

Psoriasis;
Microneedle;
Responsive release;
Drug delivery;
Oxygen;
Reactive oxygen species;
Sustained release;
Triamcinolone acetonide

Abstract Psoriasis is a prevalent chronic inflammatory skin disorder, characterized by epidermal thickening and an inflammatory hypoxic microenvironment, which significantly hinder drug penetration through the thickened skin and limit the efficacy of photodynamic therapy (PDT). Here, we introduce a dual-section microneedle (MN) patch (termed S-PTP MN patch) to enhance the therapeutic efficacy of psoriasis treatment. The needle section contains PTP nanoparticles (NPs) loaded with triamcinolone acetonide (TA) and coated with a reactive oxygen species (ROS)-responsive layer, while the base section of the patch encapsulates sodium percarbonate (SPC) particles that serve as oxygen generators to facilitate deep penetration of the PTP NPs into inflammatory sites and improve PDT efficacy. Moreover, the PTP NPs enable sustained release of TA drug over 6 days, demonstrating potent anti-inflammatory activity. In an imiquimod-induced psoriatic mouse model, a single application of the S-PTP MN patch demonstrated superior therapeutic efficacy compared to the conventional topical TA cream, with significantly

*Corresponding authors.
E-mail addresses: chengbo@znhospital.cn (Bo Cheng), huhankun@whu.edu.cn (Hankun Hu), weili.mn@whu.edu.cn (Wei Li).
[†]These authors made equal contributions to this work.

Peer review under the responsibility of Chinese Pharmaceutical Association and Institute of Materia Medica, Chinese Academy of Medical Sciences.

https://doi.org/10.1016/j.apsb.2025.09.037

alleviated clinical symptoms, reduced epidermal thickness, and lowered inflammatory cytokine levels, highlighting the potential of the S-PTP MN patch as a clinically translatable strategy for effective psoriasis therapy.

1. Introduction

Psoriasis is a prevalent immune-mediated chronic inflammatory skin disease, characterized by high recurrence rates and involvement of the skin, joints, and nails, posing significant challenges to achieving sustained clinical remission[1]. The primary pathological mechanisms include immune dysregulation and a compromised skin barriers, with hallmark features such as epidermal thickening due to excessive keratinocyte proliferation, accompanied by symptoms including erythema, scaling, dryness, and itching[2]. A wide range of therapeutic strategies have been developed for the treatment of psoriasis, ranging from topical corticosteroids[3,4], to systemic agents like methotrexate[5,6], which offer varying degrees of symptom relief. In recent years, biologic agents targeting specific immune pathways have revolutionized management of the disease, exhibiting high efficacy and improved safety profiles[7,8]. However, biologics are costly, may require long-term administration, and can increase the risk of infections. Moreover, therapeutic resistance and disease relapse remain prevalent, necessitating the exploration of adjunct or alternative strategies.

Among emerging modalities, photodynamic therapy (PDT) has garnered attention as a safe, non-invasive, and spatiotemporally selective option with minimal systemic side effects[9,10]. PDT typically involves the activation of photosensitizers by light in the presence of oxygen, resulting in the generation of cytotoxic reactive oxygen species (ROS) that selectively eliminate hyperproliferative keratinocytes in psoriatic lesions[11,12]. Despite its advantages, conventional PDT faces several limitations in the treatment of psoriasis. Firstly, the thickened stratum corneum in psoriatic skin acts as a substantial barrier, hindering the effective delivery of photosensitizers and significantly reducing therapeutic efficacy[13,14]. Furthermore, photosensitizers require oxygen to generate sufficient levels of ROS, but the hypoxic microenvironment of psoriatic lesions compromises this mechanism[15,16], limiting the effectiveness of PDT. Additionally, the psoriatic microenvironment is characterized by pronounced inflammation, including activated immune pathways and infiltrating immune cells that release pro-inflammatory cytokines, further exacerbating oxidative stress *via* excessive ROS generation[17]. Therefore, the development of a novel therapeutic strategy with enhanced drug penetration, improved PDT efficacy, and the ability to modulate the inflammatory microenvironment would be highly desirable for effective psoriasis management.

Microneedles (MNs), typically ranging from tens to hundreds of micrometers in length, have emerged as an effective transdermal drug delivery system due to their unique properties, including enhanced drug penetration, improved delivery efficiency, and increased patient compliance[18-21]. Therefore, MNs have been widely used in the treatment of various diseases, such as diabetes[22,23], wound healing[24-26], hair loss[27,28], skin cancer[29,30], and notably psoriasis[31,32]. Several recent studies have demonstrated the feasibility of MN-based platforms for psoriasis therapy. For example, Zhu's research group[33] developed a detachable H_2O_2-responsive, gel-based MN patch for psoriasis therapy. This MN patch featured a dual-mode drug release profile, enabling the rapid release of methotrexate and sustained release of epigallocatechin gallate, thereby improving therapeutic outcomes in psoriasis-like animal models. Our research group also recently reported a dissolvable MN patch incorporating self-assembled hyaluronic acid (HA) nanoparticles (NPs) conjugated with methotrexate for targeted and long-acting psoriasis treatment[34]. Despite these advancements, MNs-mediated transdermal drug delivery still suffers from limited drug penetration depth, particularly through the thickened epidermis in psoriatic skin. Additionally, mechanical resistance and skin elasticity often prevent full insertion of MNs, thereby compromising drug delivery efficiency[35]. Furthermore, the integration of MNs with PDT for psoriasis therapy remains largely unexplored.

In this work, we designed a dual-section microneedle (S-PTP MN) patch for psoriasis therapy. The patch comprises two distinct layers: (1) a tip layer composed of HA encapsulating triamcinolone acetonide (TA)-loaded, TSPBA-polyvinyl alcohol (PVA)-modified NPs (termed PTP NPs); and (2) a base layer made of polyvinylpyrrolidone (PVP) containing sodium percarbonate (SPC) particles, which serves as oxygen generators to facilitate the effective delivery of PTP NPs to the inflammatory sites and enhance PDT efficacy (Fig. 1A). SPC is a solid adduct of sodium carbonate and hydrogen peroxide. When dissolved in water, it decomposes to release hydrogen peroxide, which further breaks down into water and oxygen. Upon insertion into the thickened epidermis, the S-PTP MN patch rapidly dissolves, releasing SPC particles that react immediately with interstitial fluid to generate oxygen, which promotes deep diffusion of PTP NPs into psoriatic tissue (Fig. 1B). Within the lesion, the PTP NPs undergo responsive degradation in the ROS-rich environment, enabling efficient PDT under light irradiation, which is further enhanced by the locally elevated oxygen concentration, thereby significantly suppressing keratinocyte proliferation. Meanwhile, PTP NPs allow for the sustained release of TA drug during slow degradation, providing a potent anti-inflammatory effect. This dual-action strategy of controlled ROS generation and continuous anti-inflammatory drug release can maximize therapeutic efficacy in psoriasis treatment while maintaining favorable safety. Owing to these features, in an imiquimod (IMQ)-induced psoriatic mouse model, a single application of the S-PTP MN patch demonstrated a superior therapeutic efficacy compared to the conventional topical TA cream, with significantly alleviated clinical symptoms and reduced epidermal thickness and inflammatory cytokine levels, which highlights the potential of the S-PTP MN patch as a clinically translatable strategy for effective psoriasis therapy.

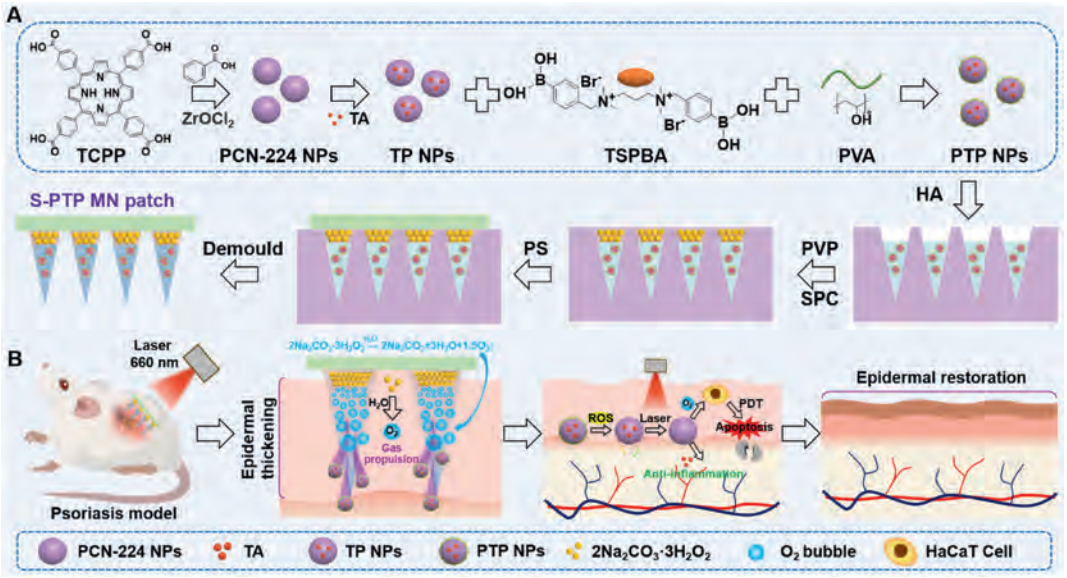

Figure 1 Schematic illustration of the preparation and application of the S-PTP MN patch for psoriasis treatment. (A) Preparation of PTP NPs and dual-sectioned S-PTP MN patch. (B) Application of the S-PTP MN patch for enhanced psoriasis therapy.

2. Materials and methods

2.1. Materials

HA (molecular weight, 10 kDa) was obtained from Meilun (Dalian, China). Tetrakis (4-carboxyphenyl) porphyrin (TCPP), zirconyl chloride octahydrate ($ZrOCl_2 \cdot 8H_2O$), benzoic acid (BA), DPBF, *N*,*N*-dimethylformamide (DMF), and ethanol were purchased from Macklin Biochemical Technology Co. (Shanghai, China). DMEM, fetal bovine serum (FBS), and penicillin−streptomycin antibiotics were sourced from Gibco (New York, NY, USA). MTT, live/dead cell staining kit, and cytotoxicity assay kit were procured from Beyotime (Shanghai, China). Phosphate-buffered saline (PBS) was obtained from Service Bio (Wuhan, China).

2.2. Methods

2.2.1. Characterization of PTP NPs and S-PTP MN patch

The crystal structure of PTP NPs was characterized by XRD. The microstructure of the NPs was examined using transmission electron microscopy (TEM, Hitachi, HT7700, Hitachi Ltd., Tokyo, Japan). The particle size and zeta potential of PTP NPs were measured by Nanoparticle Size and Zeta Potential Analyzer. UV−Vis spectra of PTP were recorded with a UV−visible spectrophotometer. The infrared absorption peaks of the samples were recorded using an FTIR spectrometer (Thermo Fisher, Nicolet iS50, Waltham, USA). Thermogravimetric analysis (TGA, Mettler-Toledo, TGA2/DSC3, Mettler-Toledo International Inc., Columbus, USA) was conducted to characterize the thermal properties of PTP. The morphology of the MN patches was observed with scanning electron microscopy (SEM, Hitachi SU8010, Hitachi Ltd., Tokyo, Japan) and an optical microscope (LEICA TL3000Ergo, Wetzlar, Germany). The mechanical strength of the MN patches was assessed using a mechanical tester (Mark-10, ESM303, New York, USA). Fluorescence images were captured with an inverted fluorescence microscope (Olympus, IX73, Tokyo, Japan).

2.2.2. Synthesis of PCN-224 NPs

PCN-224 NPs were synthesized using a solvothermal method. First, 100 mg of TCPP, 200 mg of $ZrOCl_2 \cdot 8H_2O$, and 2.8 g of BA were dissolved in 100 mL dimethylformamide (DMF) and thoroughly dispersed. The mixture was then left undisturbed in a dark oven at 90 °C for 5 h. Afterward, it was centrifuged at 11,000 rpm for 20 min to collect the precipitate. The precipitate was washed three times with DMF and then vacuum-dried overnight at 80 °C to obtain the final PCN-224 NPs.

2.2.3. Synthesis of TSPBA

The amount of 1.5 g (4-bromomethylphenyl) boronic acid was dissolved in 60 mL DMF at 60 °C, after which 0.15 g of *N*,*N*,*N*′,*N*′-tetramethyl-1,3-propanediamine was added to the mixture and stirred for 24 h. Following the addition of 150 mL of tetrahydrofuran (THF) to the solution, the mixture was quickly filtered. The resulting precipitate was washed three times with THF and then vacuum-dried overnight at 40 °C to yield pure TSPBA.

2.2.4. Synthesis of PTP NPs

A total of 10 mg PCN-224 NPs and 20 mg of TA were added to 5 mL of acetone and stirred at room temperature for 24 h. The mixture was then centrifuged at 11,000 rpm for 20 min, and the resulting precipitate was washed three times with acetone to remove any unencapsulated TA. Finally, the precipitate was vacuum dried at 40 °C to yield TP NPs. Subsequently, 10 mg of TP NPs was added to a 2 mL solution containing 2% PVA and 2% TSPBA, and the mixture was ultrasonicated for 5 min to ensure uniform dispersion. The suspension was centrifuged at 11,000 rpm, and the precipitate was washed three times with deionized water before being freeze-dried to obtain PTP NPs.

2.2.5. Release of TA from PTP NPs in vitro

To evaluate the release of TA from PTP NPs *in vitro*, 10 mg of PTP NPs was placed in a dialysis bag and dispersed in 10 mL Tri-HCl buffer release medium at 37 °C. The experimental group used a release medium containing 400 μmol/L H_2O_2 to better mimic the oxidative stress conditions associated with psoriatic pathology[33,36]. They were then placed together on a shaker at 150 rpm. At the predetermined time points (0, 8, 12, 24, 48, 72, 96, 120, 144, and 168 h), 1 mL of supernatant was collected and 1 mL of fresh release medium was added to maintain the constant volume. The UV−Vis absorbance of the sample was measured at 240 nm and the cumulative release rate of TA was calculated.

2.2.6. Evaluation of ROS generation by PTP NPs through photodynamic action

DPBF was used as a probe to measure ROS generation. Briefly, 60 μmol/L DPBF solution was prepared by using the solvent of DMF. Then, 8 μL of the DPBF solution was added to a sample suspension dispersed in 992 μL of DMF to obtain a 100 μg/mL PTP dispersion. The sample was irradiated with a 660 nm laser, and supernatant samples were collected at the time points of 0, 1, 2, 3, 4, and 5 min. The UV−Vis absorbance of the collected samples was measured at 415 nm.

2.2.7. Fabrication and characterization of S-PTP MN patches

The MN patches were fabricated using a three-step casting process with a polydimethylsiloxane (PDMS) mold. First, 100 μL of 16% HA (10 kDa) and 16% sucrose aqueous solution, mixing with 10 mg/mL PTP NPs, filled into the tips of the MN mold by centrifugation (4200 rpm, 5 min). The mold was then air-dried at room temperature overnight to form the needle-tip layer. For the base layer, 3% SPC was added to a 30% PVP (55 kDa) ethanol solution and filled into the mold. Finally, 50 μL PS (20%) solution dissolved in dioxane was casted on the mold surface to form the backing layer. The mold was then dried at room temperature for 24 h, and the MN patch was carefully peeled from the mold, yielding the S-PTP MN patch, which was stored in a desiccator for future use. Blank MN patches were fabricated by casting solutions without PTP and SPC, following the same method as S-PTP MN patch. The morphology of the MNs was observed and imaged using SEM and optical microscopy.

2.2.8. Skin penetration and mechanical performance tests of the S-PTP MN patch

The S-PTP MN patch was applied to porcine skin *ex vivo* for 15 min. Afterward, delivered drug in the skin was observed under an optical microscope, and the residual MN patch was collected and photographed. The skin was then sectioned into 10-μm thick slices using a cryostat (Thermo Fisher Scientific, HM525 NX, Waltham, USA) and imaged under an inverted fluorescence microscope to observe the cross-section of the skin. Finally, a mechanical tester was used to measure the deformation stress of a single needle to verify the puncture performance of the S-PTP MN.

2.2.9. Evaluation of cellular uptake of PTP NPs

HaCaT cells were seeded into six-well plates and cultured in DMEM containing 10% FBS and 1% antibiotics at 37 °C in an incubator with 5% CO_2 for 24 h. The cells were then placed in an anaerobic pouch for 6 h to induce hypoxia in HaCaT cells. Different MNs were added to the cells for co-incubation, and at the time points of 0, 2, 4, and 8 h, the cells were washed three times with PBS and stained with DAPI for nuclear visualization. The fluorescence intensity within the cells was observed under an inverted fluorescence microscope.

2.2.10. Evaluation of intracellular ROS generation by PTP NPs

After co-incubation with MNs and subsequent laser treatment, intracellular singlet oxygen production was assessed using a DCFH-DA detection kit, and the fluorescence intensity within the cells was observed under an inverted fluorescence microscope.

2.2.11. Cytotoxicity and biosafety evaluation of S-PTP MN patches

HaCaT cells were used to assess cytotoxicity of the MN patches. The toxicity of biomaterials in the MN patch-treated and untreated groups was evaluated using the MTT assay and a calcein-AM/PI staining kit. Each experiment was performed in triplicate. To further assess the biocompatibility of PTP NPs and MN patches, rat blood was collected in anticoagulant tubes. Blood samples were centrifuged at 1500 rpm for 15 min at 4 °C to collect red blood cells (RBCs), which were then dispersed in normal saline solution. A 200 μL RBC suspension was mixed with normal saline solution containing PTP or MN patches. Normal saline solution and ultrapure water were used as negative and positive controls, respectively. The cell suspensions were incubated at room temperature for 4 h, and then centrifuged at 3000 rpm for 10 min. The absorbance of the supernatant was measured at 540 nm using a UV spectrophotometer to calculate the hemolysis rate.

2.2.12. Therapeutic efficacy of the S-PTP MN patch for psoriasis treatment in vivo

The experimental protocol was approved by the Animal Care and Use Committee of Wuhan University (WP20240380). SPF-grade male BALB/c mice (18−20 g) were used to evaluate the therapeutic efficacy of MN patches in a psoriasis-like mouse model. After a 7-day acclimation period, the mice were randomly divided into seven groups ($n = 5$) for different treatments: Health, Model, TA cream, PTP MN (L), S-PP MN (L), S-PTP MN and S-PTP MN (L). The hair on the mice's backs was removed, and 62.5 mg of IMQ cream was applied daily for 7 consecutive days to induce a psoriasis-like dermatitis model. Treatment was initiated immediately after successful model establishment, and skin photographs of the mice's backs were taken on Days 1, 3, 5, and 7 under a microscope to assess healing progress. After 7 days of treatment, the mice were euthanized, and skin samples were collected and processed into paraffin sections for histological analysis. ImageJ software was used to quantify psoriasis skin thickness, positive rates of IL-6, IL-17, IL-23, and TNF-α, as well as Ki67 fluorescence indicators. Finally, the major organs (heart, liver, spleen, lungs, and kidneys) were collected from the mice and stained with H&E to evaluate *in vivo* biosafety.

2.2.13. Statistical analysis

The experimental results in this study are presented as mean ± standard deviation (SD). Statistical analysis was performed using a two-sided Student's *t*-test or ANOVA. Origin and GraphPad software were used for the statistical analyses. A *P*-value of less than 0.05 was considered statistically significant, with significance levels indicated as $*P < 0.05$, $**P < 0.01$, $***P < 0.001$.

3. Results and discussion

3.1. Preparation and characterization of PTP NPs

Triamcinolone acetonide (TA) was initially encapsulated into PCN-224 NPs *via* physical adsorption to form TP NPs. Subsequently, a ROS-responsive P-T coating (PVA modified with TSPBA, *i.e.*, PVA-TSPBA) was applied to the surface through ultrasonic stirring, resulting in the formation of PTP NPs. Transmission electron microscopy (TEM) revealed that the PTP NPs maintained a spherical morphology with size and structure comparable to PCN-224 (Fig. 2A and B). X-ray diffraction (XRD) analysis confirmed the purity and crystallinity of the PTP NPs, exhibiting characteristic peaks at 4.65°, 6.54°, 7.99°, and 9.22° that aligned with reported PCN-224 data, indicating successful synthesis and structural preservation after TA loading and P-T coating (Fig. 2C). Thermogravimetric analysis (TGA) demonstrated a TA loading efficiency of approximately 9.80 ± 0.61% (Fig. 2D). Elemental composition analysis *via* X-ray photoelectron spectroscopy (XPS) revealed the presence of Zr, Br, B, F, C, and O, further confirming the successful integration of TA and the P-T coating in the PTP NPs (Fig. 2E and F). Fourier transform infrared (FTIR) spectroscopy of PCN, P-T, and PTP samples showed that PTP NPs exhibited distinct absorption peaks corresponding to the C═O bond at 1690 cm^{-1} and the B-O-C bond at 1101 cm^{-1} (Fig. 2G), consistent with the characteristic signals of PCN and P-T, thereby validating the successful synthesis of PTP NPs. Dynamic light scattering (DLS) analysis indicated that the average particle size of PTP NPs was 298.07 ± 3.85 nm, larger than that of TP NPs (187.93 ± 5.87 nm), due to the presence of the P-T coating (Fig. 2H and I). Additionally, zeta potential measurements showed a decrease from 26.73 ± 0.90 mV to 1.97 ± 0.51 mV after P-T coating (Fig. 2J), supporting successful surface modification.

To simulate the release behavior of TA in a psoriatic lesion environment, the *in vitro* release of TA from PTP NPs was assessed under ROS conditions. As shown in Fig. 2K, the release of TA was significantly accelerated in a medium containing 400 μmol/L hydrogen peroxide (H_2O_2), with a cumulative release reaching 90% by Day 6. This suggests that PTP NPs can achieve ROS-responsive drug release in the high-ROS environment characteristic of psoriatic lesions. Both the ROS-responsive condition (400 μmol/L H_2O_2) and the normal condition (without H_2O_2) exhibited a notable initial burst release, with approximately 30% of the total drug released at the first time point of 5 h. This rapid initial release is likely attributed to TA molecules located near or on the surface of the PTP NPs, which are more readily diffused upon exposure to aqueous media. Furthermore, PTP NPs pretreated with H_2O_2 demonstrated strong ROS generation upon 660 nm light irradiation (Fig. 2L and Supporting Information Fig. S1), indicating that the TA-loaded and P-T-coated NPs retained their photodynamic capabilities.

3.2. Preparation and characterization of the S-PTP MN patch

To enhance the delivery efficiency of PTP NPs, we incorporated them into a double-layered MN patch, termed the S-PTP MN patch, using a three-step casting method. The needle tip layer was

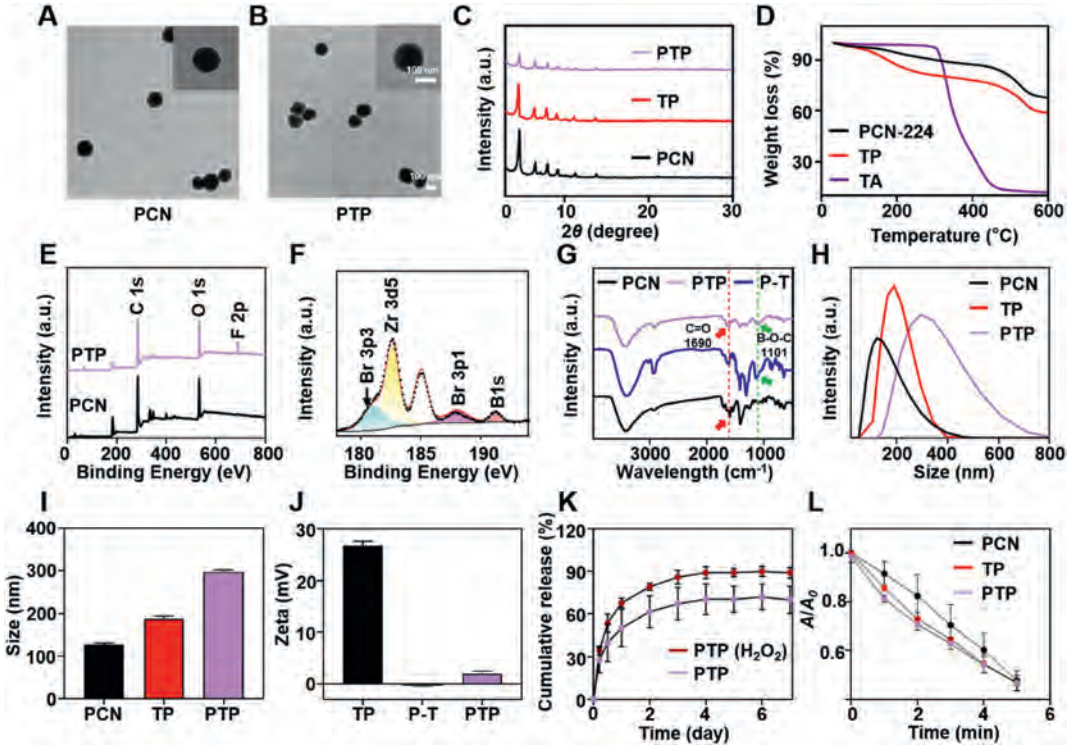

Figure 2 Synthesis and characterization of PTP NPs. TEM images of PCN-224 NPs (A) and PTP NPs (B). (C) XRD analysis of PCN-224, TP and PTP NPs. (D) TGA curves of PCN-224, TP, and TA. (E, F) XPS analysis of PCN, TP and PTP NPs. (G) FT-IR spectra of PCN, P-T and PTP. (H, I) Particle size of PCN, TP and PTP NPs. (J) Zeta potential of PCN, P-T and PTP. (K) Cumulative *in vitro* release of TA from the PTP NPs with or without H_2O_2. (L) Comparison of DPBF normalized degradation rate (A/A_0) of PCN-224, TP, and PTP NPs after laser irradiation. $n = 3$ independent samples. Data are presented as mean ± SD.

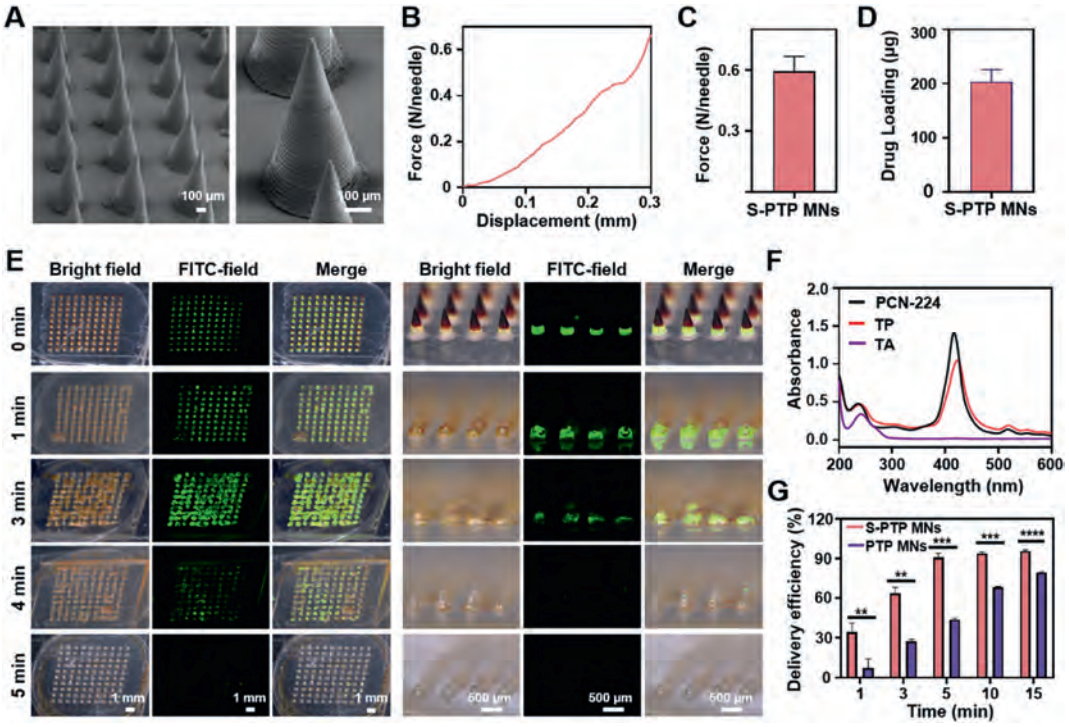

Figure 3 Synthesis and characterization of the S-PTP MN patch. (A) SEM images of the S-PTP MN patch. (B, C) The mechanical characterization of the S-PTP MNs. (D) Drug loading of the S-PTP MN patch. (E) The dissolution process of S-PTP MNs in porcine skin *ex vivo* within 5 min. (F) UV absorption curves of TA, TP and PCN-224. (G) Drug delivery efficiency of the TP MN patch and S-TP MN patch, respectively. $n = 3$ independent samples, $^{**}P < 0.01$, $^{***}P < 0.001$, $^{****}P < 0.0001$. Data are presented as mean ± SD.

composed of HA polymer and PTP NPs, while the base layer comprised SPC particles and PVP polymer. As shown in the scanning electron microscope (SEM) image (Fig. 3A), the MN tips exhibited a conical shape and were arranged in a 10 × 10 array on a 7 mm × 7 mm backing, with each needle measuring 850 μm in height. Mechanical testing revealed a puncture failure force of 0.59 ± 0.07 N per needle (Fig. 3B and C), greater than the required minimal force of 0.058 N[37], indicating that the S-PTP MN patch had sufficient mechanical strength for skin penetration and drug delivery. Each patch contained 203.64 ± 21.63 μg of NPs (Fig. 3D), as determined by UV absorbance at 420 nm (Fig. 3F).

To facilitate visualization, the base layer of the S-PTP MN patch was loaded with fluorescein isothiocyanate (FITC) dye and applied to porcine skin *ex vivo* (Fig. 3E). The results showed that the S-PTP MNs rapidly dissolved upon insertion, driven by the propulsion of oxygen bubbles generated from the patch. As shown in Fig. 3G, the S-PTP MN patch achieved over 90% drug delivery efficiency within 5 min, approximately twice that of the control group (*e.g.*, PTP MNs), demonstrating a significantly enhanced capacity for transdermal drug delivery.

3.3. SPC facilitates evaluation of drug delivery behavior of the S-PTP MN patch

We first evaluated the oxygen-generating capability of S-PTP MNs *in vitro*. As illustrated in Fig. 4A, the S-PTP MNs rapidly dissolved upon contact with phosphate-buffered saline (PBS), producing abundant oxygen bubbles at the base layer, which facilitated the diffusion of PTP NPs. Quantitative analysis revealed that the diffusion distance of PTP NPs from S-PTP MNs was approximately 2.6 times greater than that observed with PTP MNs lacking SPC in the base layer (Fig. 4B). Moreover, dissolved oxygen measurements confirmed that S-PTP MNs continuously generated ~20 mg/L of oxygen within 1 h in PBS, whereas no oxygen generation was detected from PTP MNs (Fig. 4C).

We then evaluated the transdermal diffusion depth of the therapeutic NPs following S-PTP MN application. As shown in Fig. 4D, both PTP and S-PTP MNs effectively penetrated porcine skin in an *ex vivo* model. However, S-PTP MNs achieved significantly greater penetration depth compared to PTP MNs (443.31 ± 30.13 μm *vs.* 303.11 ± 24.77 μm), likely due to the oxygen-generating reaction between SPC and interstitial fluid upon insertion (Fig. 4E). Additionally, post-application analysis revealed minimal residual drug in the used S-PTP patches, further confirming efficient transdermal delivery (Supporting Information Fig. S2).

To further validate the enhanced penetration performance, we examined S-PTP MNs in a psoriatic mouse skin model *ex vivo*, where the skin is typically thickened and poses a barrier to transdermal drug delivery[38]. As shown in Fig. 4F, PTP MNs exhibited limited penetration, whereas S-PTP MNs effectively delivered PTP NPs into the thickened psoriatic skin, achieving a significantly greater penetration depth (427.71 ± 11.80 μm *vs.* 231.91 ± 5.87 μm), nearly double that of the PTP MNs (Fig. 4H). This enhanced delivery performance was further corroborated by confocal laser scanning microscopy (CLSM), which visualized the deeper and more uniform nanoparticle distribution achieved by S-PTP MNs (Fig. 4G).

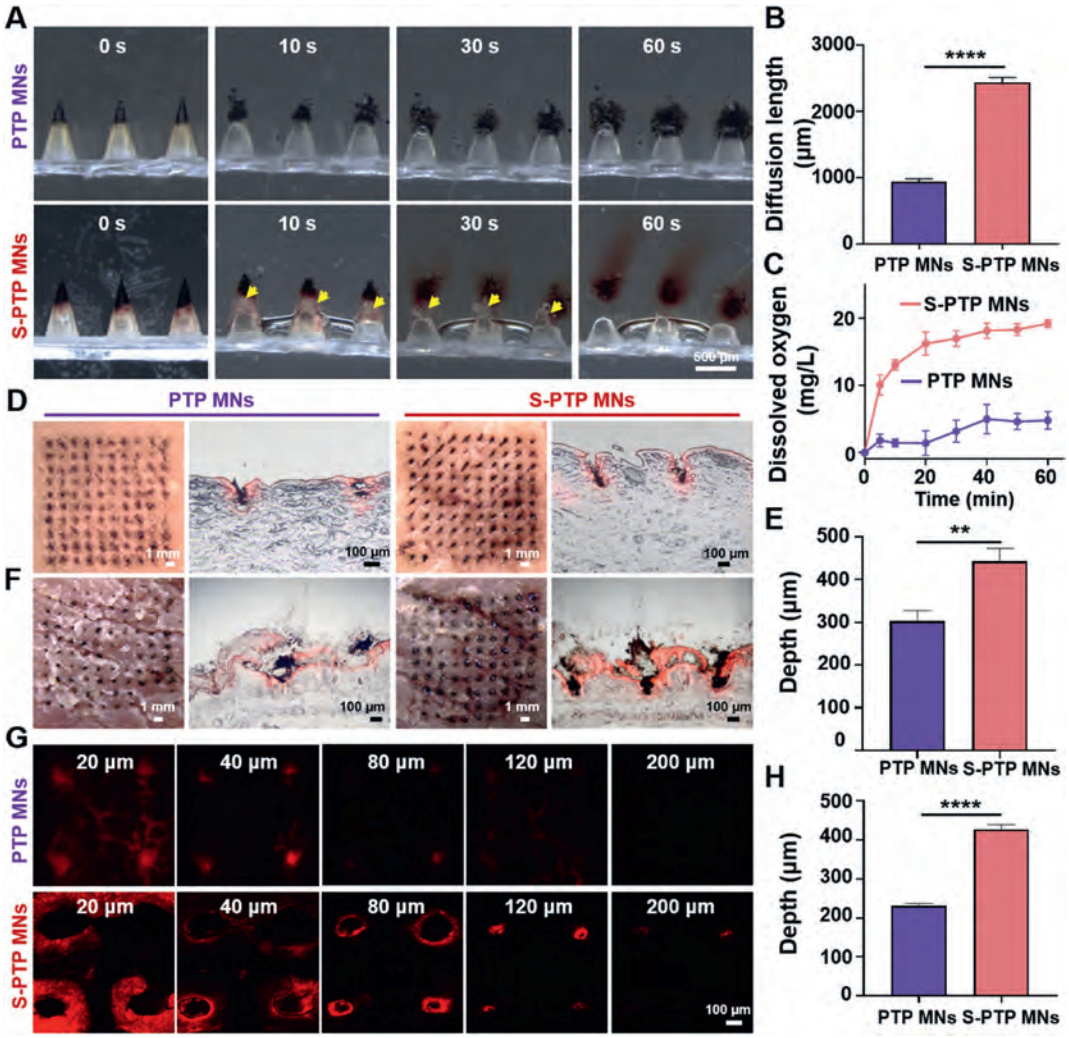

Figure 4 Evaluation of drug penetration *via* the S-PTP MNs *in vitro* and *ex vivo*. (A) Drug diffusion of PTP MNs or S-PTP MNs in PBS. (B) Diffusion distance analysis of PTP MNs and S-PTP MNs in PBS. (C) The concentration of oxygen generated by PTP MNs or S-PTP MNs over time. Skin images and frozen section images of PTP MNs and S-PTP MNs after puncture in porcine skin *ex vivo* (D) or psoriatic mouse skin *ex vivo* (F). Puncture depth analysis of PTP MNs and S-PTP MNs in porcine skin *ex vivo* (E) or psoriatic mouse skin *ex vivo* (H). (G) Fluorescent CLSM images of porcine skin treated by PTP MNs or S-PTP MNs. $n = 3$ independent samples, $^{**}P < 0.01$, $^{****}P < 0.0001$. Data are presented as mean ± SD.

3.4. Cellular uptake of PTP NPs and photodynamic performance of the S-PTP MN patch

We next investigated the cellular uptake of NPs and the photodynamic activity of the S-PTP MN patch *in vitro*. HaCaT cells were exposed to hypoxic conditions and subsequently co-incubated with various MN formulations. After incubation for 8 h, fluorescence staining was performed to assess the uptake of PTP NPs by HaCaT cells. As shown in Fig. 5A and B, co-incubation with S-PTP MNs and H_2O_2 resulted in significantly increased NP uptake compared to S-PTP MNs alone, exhibiting levels similar to those observed in the S-TP MN group. This increased uptake is likely due to the ROS-triggered degradation of the P-T coating, leading to the release of smaller-sized TP NPs, which facilitates cellular internalization and explains the comparable uptake seen with the S-TP MNs.

Upon irradiation with a 660 nm near-infrared (NIR) laser, PTP catalyzes the conversion of molecular oxygen (O_2) into singlet oxygen ($^1O_2$), inducing apoptosis in hyperproliferative keratinocytes. To assess the photodynamic therapeutic potential of S-PTP MNs, HaCaT cells were incubated with various MN formulations for 24 h. Cell viability was evaluated using the MTT assay. Notably, the S-PTP MN (H/L) group that was treated with both H_2O_2 and NIR irradiation, exhibited an inhibition rate exceeding 84%, indicating potent antiproliferative effects (Fig. 5C). These results were consistent with the findings from live/dead cell staining (Fig. 5D).

Intracellular reactive oxygen species (ROS) generation was further assessed using the DCFH-DA fluorescent probe. Both the S-PTP MN (H/L) and S-TP MN (L) groups showed markedly elevated ROS levels compared to other groups (Fig. 5E), highlighting the role of ROS in facilitating NP uptake and enhancing photodynamic efficacy. These observations were supported by flow cytometry analysis, which revealed a significant increase in apoptosis among HaCaT cells in the S-PTP MN (H/L) group (Fig. 5F and G).

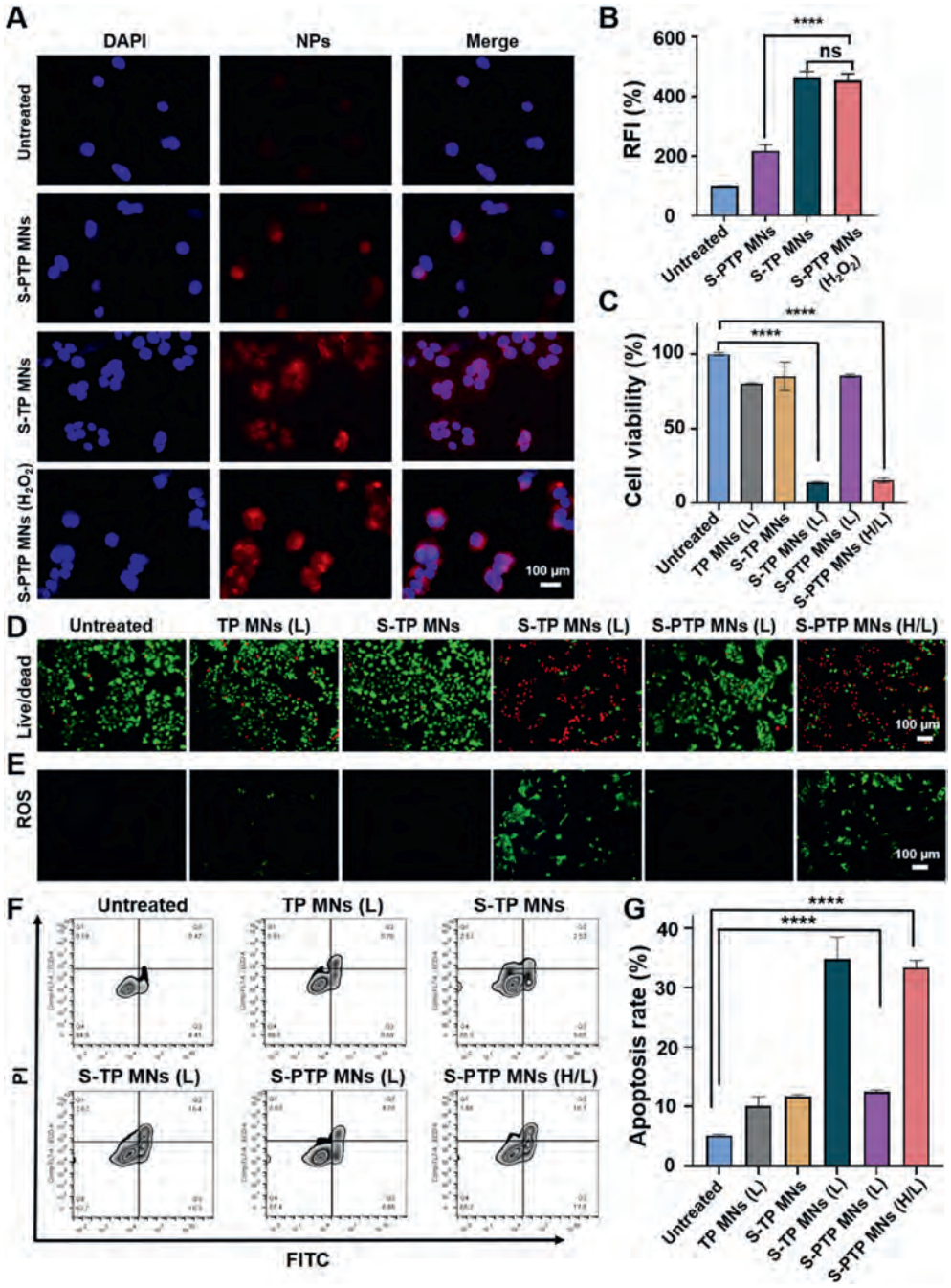

Figure 5 Evaluation of MN therapy *in vitro*. (A) The uptake fluorescence image of NPs in HaCaT cells co-incubated with different MNs for 8 h. (B) Relative fluorescence intensity of PTP NPs after cellular uptake. (C) Viability of HaCaT cells after receiving different treatments. (D) Calcein-AM/PI staining of HaCaT cells after receiving different treatments. (E) Fluorescence of intracellular ROS within HaCaT cells after receiving different treatments. (F) The flow cytometry distribution plot illustrating the percentage of apoptosis in HaCaT cells after receiving different treatments. (G) Analysis of the apoptosis rate of HaCaT cells. $n = 3$ independent samples, $^{****}P < 0.0001$. ns, not significant. Data are presented as mean ± SD.

3.5. Biosafety evaluation of the S-PTP MN patch

To evaluate the biocompatibility and biosafety of S-PTP MN patch, human umbilical vein endothelial cells (HUVECs) and NIH/3T3 cells were used as *in vitro* models. Cytotoxicity was first assessed using live/dead cell staining, where live cells were labeled with green fluorescence (Calcein-AM) and dead cells with red fluorescence (propidium iodide, PI). As shown in Supporting Information Fig. S3, after 24 h of co-culture with the S-PTP MN patch, both HUVECs and NIH/3T3 cells displayed predominantly

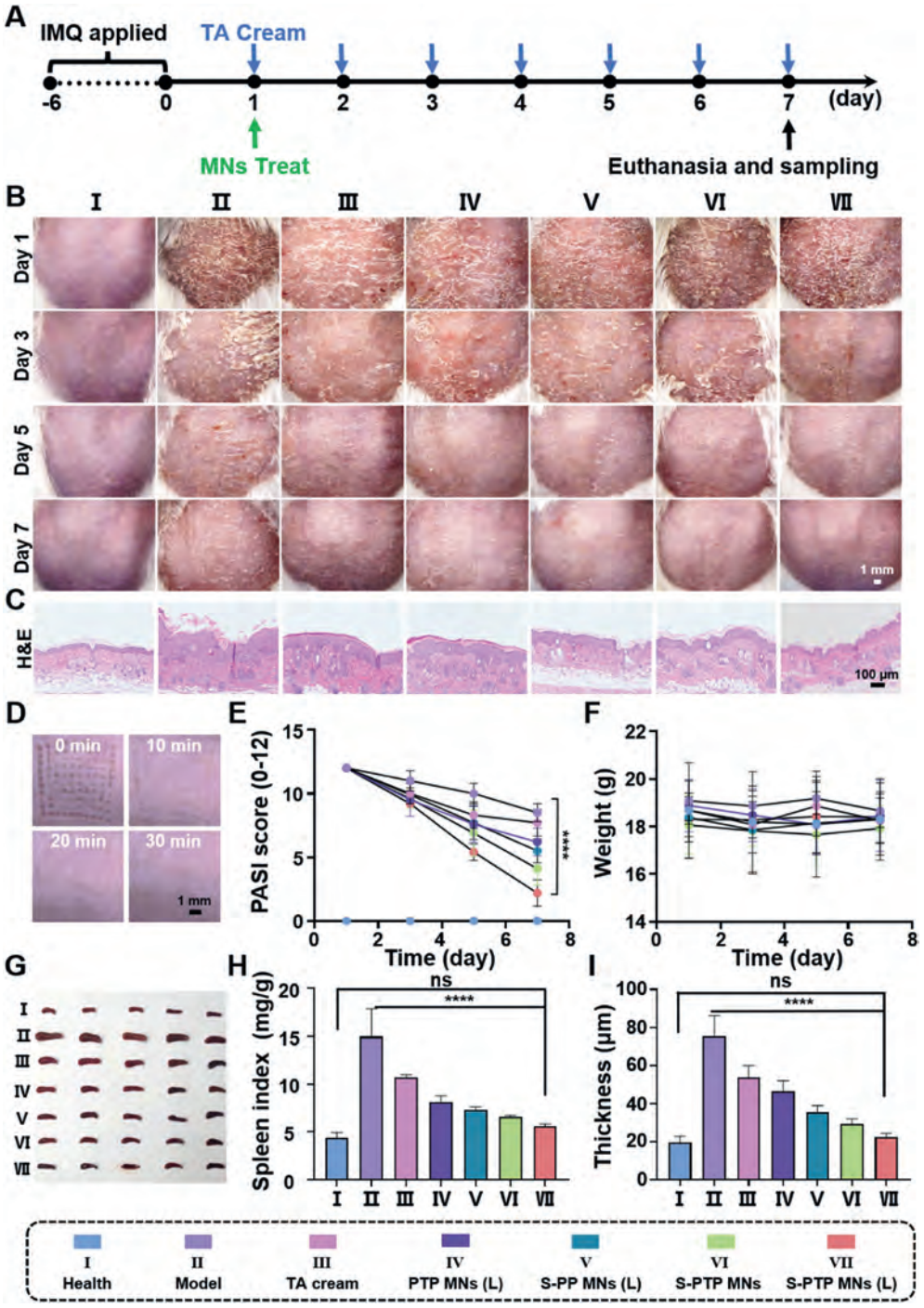

Figure 6 Therapeutic efficacy of S-PTP MN patch on psoriasis treatment *in vivo*. (A) Experimental design of psoriasis treatment. (B) Representative photographs of mouse back skin on Days 1, 3, 5 and 7 in different groups. (C) Representative H&E staining images of mouse skin in different groups. (D) Images of mouse skin recovery within 30 min after application of a S-PTP MN patch. (E) Total PASI scores of mice in different groups. (F) Changes in average body weight of mice in different groups. Optical photographs of the spleen (G) and spleen index (spleen weight/mouse weight) (H) in different groups. (I) Epidermis thickness of mouse skin after receiving different treatments. $n = 5$ independent samples, $^{****}P < 0.0001$. ns, not significant. Data are presented as mean ± SD.

green fluorescence, comparable to that of untreated controls, indicating excellent biocompatibility. Furthermore, a hemolysis assay was conducted to assess blood compatibility. The hemolysis rate remained below 5% (Supporting Information Fig. S4), further confirming the favorable biosafety of the S-PTP MN patch.

3.6. Therapeutic efficacy of the S-PTP MN patch for psoriasis treatment in vivo

To assess whether the prolonged release could be replicated *in vivo*, we encapsulated the fluorescent dye Rhodamine 123—a

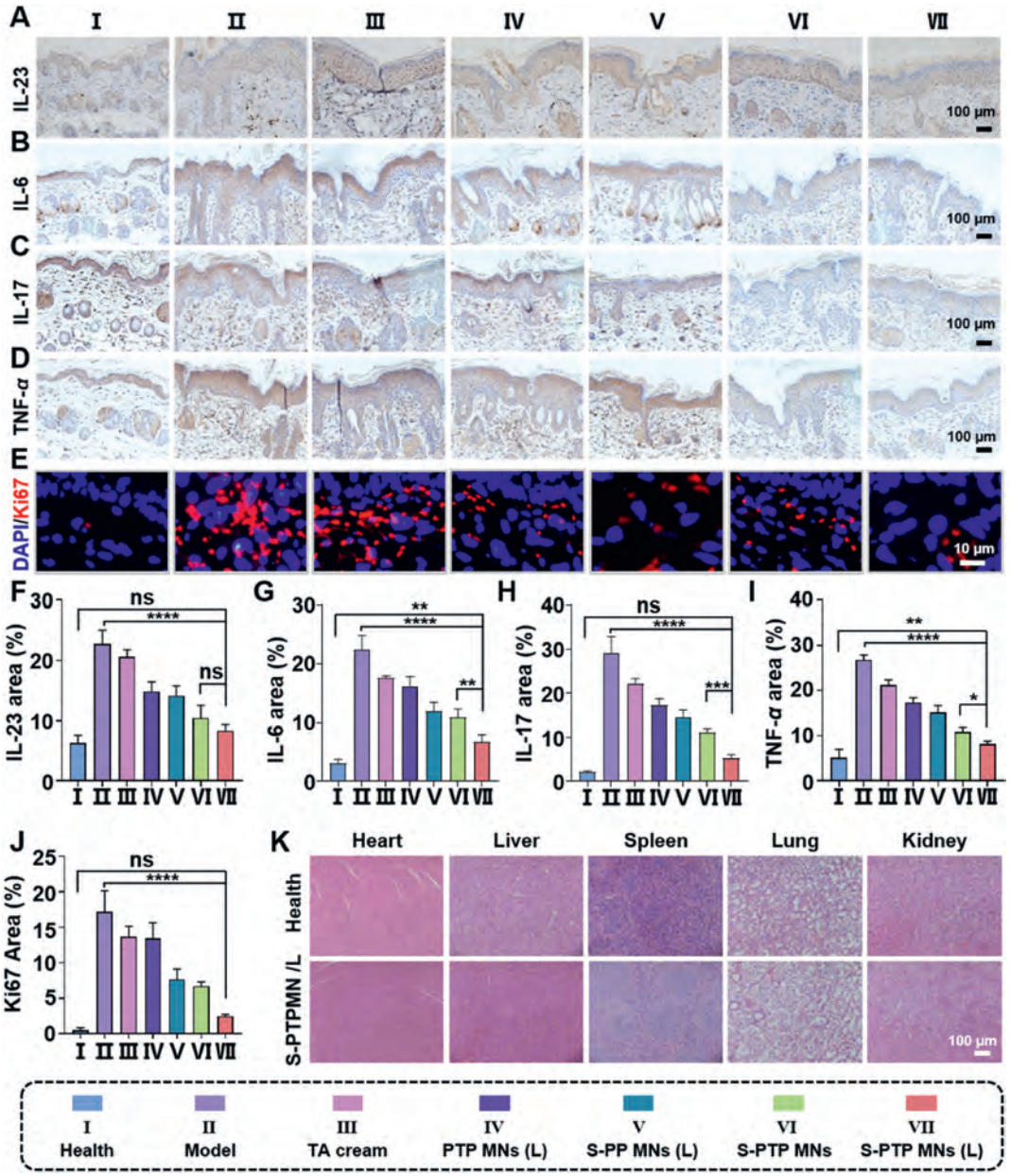

Figure 7 Anti-inflammatory and anti-cell proliferation effects of the S-PTP MN patch in the treatment of psoriasis *in vivo*. Immunohistochemical staining of IL-23 (A), IL-6 (B),IL-17 (C), and TNF-α (D). (E) Representative fluorescence staining images of Ki67 in the skin of mice in different groups. Statistical evaluation of positive area of IL-23 (F), IL-6 (G), IL-17 (H), and TNF-α (I). (J) Statistical evaluation of Ki67 positive area in each group. (K) Representative H&E staining images of the heart, liver, spleen, lung, and kidney of mice in the health group and the S-PTP MN/L group on day 7. $n = 5$ independent samples, $^{*}P < 0.05$, $^{**}P < 0.01$, $^{***}P < 0.001$, $^{****}P < 0.0001$. ns, not significant. Data are presented as mean ± SD.

hydrophobic molecule used to mimic the physicochemical properties of TA—within the NPs. As presented in Supporting Information Fig. S5, the fluorescently labeled NPs were efficiently delivered into the psoriatic skin of mice *via* the MNs. Over time, a gradual decrease in fluorescence intensity was observed, likely due to the degradation of the NPs and controlled release of Rhodamine 123. Importantly, fluorescence signals remained detectable for about six days post-administration, indicating that the NPs are capable of sustaining drug release within the skin over a similar time frame *in vivo*.

To next evaluate the *in vivo* therapeutic efficacy of MNs, an imiquimod (IMQ)-induced psoriasis model was established on the dorsal skin of mice, with the lesion skin area of 2 cm × 2 cm (Fig. 6A). The mice were then randomly divided into seven groups, each receiving a different treatment: (1) Healthy control, (2) Model (IMQ only), (3) TA cream, (4) PTP MN (L), (5) S-PP MN (L), (6) S-PTP MN, and (7) S-PTP MN (L). The treated dorsal skin was monitored over time to assess clinical outcomes. The drug dose delivered by the MNs was equivalent to that of the topical TA cream, with both formulations containing 21 μg of TA.

The drug delivery efficiency of S-PTP MNs achieved 90.28 ± 2.28% *in vivo*. As illustrated in Fig. 6B, mice in the Model group developed prominent skin thickening, erythema, and scaling, confirming successful establishment of psoriasis-like dermatitis. In contrast, treatment with the S-PTP MN patch combined with laser irradiation markedly alleviated these symptoms, as evidenced by gross skin morphology (Fig. 6B) and hematoxylin-eosin (H&E) staining (Fig. 6C). Notably, skin thickness in the S-PTP MN (L) group was significantly reduced to 22.35 ± 1.95 μm, compared to 75.44 ± 10.78 μm in the Model group (Fig. 6C and I).

Psoriasis Area and Severity Index (PASI) scores were also assessed (Fig. 6E), which revealed that the S-PTP MN (L) group demonstrated the most significant improvement, with a PASI score of 2.20 ± 1.04 after 7 days, markedly lower than that of the Model group (8.50 ± 0.71). Given that IMQ-induced psoriasis often causes splenomegaly due to systemic inflammation, spleen weights were evaluated across groups. Mice in the S-PTP MN (L) group showed a substantial reduction in spleen size, with a spleen index of 5.58 ± 0.24 mg/g, approaching normal values, as compared to 14.94 ± 2.92 mg/g in the Model group (Fig. 6G and H), which suggested effective systemic anti-inflammatory effects of the treatment. Moreover, the closure of micropores in mouse skin was tested following MNs puncture, which showed that micropores disappeared within 30 min without adverse reactions (Fig. 6D). Additionally, there was no significant differences of body weights among the mice in the seven groups (Fig. 6F), indicating good biosafety of the S-PTP MN patch. To further assess pathological changes, immunohistochemistry and immunofluorescence analyses were conducted to evaluate the expression of psoriasis-related inflammatory markers. Psoriatic skin is typically characterized by elevated levels of inflammatory cytokines. However, the S-PTP MN (L) group exhibited the lowest expression of key cytokines, including IL-23 (Fig. 7A and F), IL-6 (Fig. 7B and G), IL-17 (Fig. 7C and H), and TNF-α (Fig. 7D and I), confirming the superior anti-inflammatory efficacy of the treatment.

Moreover, the expression of Ki67, a nuclear proliferation marker indicative of keratinocyte hyperproliferation, was significantly reduced in the S-PTP MN (L) group (Fig. 7E and J), further supporting the therapeutic potential of the S-PTP MN patch in suppressing epidermal hyperplasia associated with psoriasis. Finally, we assessed the biosafety of the S-PTP MN patch *in vivo* by investigating the pharmacokinetic profile of TA drug after the application of the patch in mice. The results showed that systemic TA levels remained extremely low, consistently near the detection limit of the ELISA assay (0.1 ng/mL) (Supporting Information Fig. S6), indicating highly localized drug delivery and minimal systemic absorption of the TA drug. Additionally, major organs were harvested for histopathological evaluation, and no significant inflammation or organ damage was observed in the S-PTP MN (L) group compared to untreated controls (Fig. 7K), further underscoring the favorable safety profile of this treatment approach.

4. Conclusions

Psoriasis is a chronic inflammatory skin disorder characterized by keratinocyte hyperproliferation and immune dysregulation, posing challenges for effective transdermal drug delivery due to the thickened stratum corneum. In this study, we developed a ROS-responsive, oxygen-propelling MN (S-PTP MN) patch for enhanced transdermal delivery of therapeutic drugs for targeted psoriasis treatment. TA was encapsulated within a photosensitizer-based MOF (PCN-224) and coated with a ROS-sensitive P-T shell to form PTP NPs, enabling both photodynamic therapy and responsive drug release. The S-PTP MN patch was designed as a double-layered structure: a tip layer containing PTP NPs for localized drug delivery and a base layer incorporating SPC particles for *in situ* oxygen generation. The generated oxygen bubbles not only significantly enhanced the diffusion and penetration of the therapeutic agents, achieving deeper delivery in both normal and psoriatic skin models, but also served as a fuel source, thereby amplifying the photodynamic therapeutic effect. In an IMQ-induced psoriasis mouse model, S-PTP MNs effectively alleviated clinical symptoms, reduced epidermal thickness and inflammatory cytokine levels, and showed no systemic toxicity, highlighting their potential as a promising therapeutic strategy for psoriasis.

Acknowledgments

This work was supported by the National Natural Science Foundation of China (NSFC, Nos. 82373798 and 52103182).

Author contributions

Yaqi Yuan: Conceptualization, Formal analysis, Investigation, Methodology, Validation, Writing original draft. Peng Jiang: Formal analysis, Investigation, Methodology, Validation, Writing original draft. Chuan Xiao: Methodology, Writing original draft. Jiapeng Lei: Investigation, Methodology. Bo Cheng: Supervision, Review & editing manuscript. Hankun Hu: Funding acquisition, Supervision, Review & editing manuscript. Wei Li: Conceptualization, Funding acquisition, Project administration, Supervision, Validation, Review & editing manuscript.

Conflicts of interest

The authors have no conflicts of interest to declare.

Appendix A. Supporting information

Supporting information to this article can be found online at https://doi.org/10.1016/j.apsb.2025.09.037.

References

1. Griffiths CEM, Armstrong AW, Gudjonsson JE, Barker J. Psoriasis. *Lancet* 2021;**397**:1301−15.
2. Wu XK, Ma YS, Wang L, Qin XM. A route for investigating psoriasis: from the perspective of the pathological mechanisms and therapeutic strategies of cancer. *Int J Mol Sci* 2023;**24**:14390.
3. Engel PV, Smith B, Javadi SS, Wu JJ. It is time to consider a new topical algorithm for psoriasis. *J Am Acad Dermatol* 2024;**90**:e89−90.
4. Raharja A, Mahil SK, Barker JN. Psoriasis: a brief overview. *Clin Med (Lond)* 2021;**21**:170−3.
5. van Huizen AM, Sikkel R, Caron AGM, Menting SP, Spuls PI. Methotrexate dosing regimen for plaque-type psoriasis: an update of a systematic review. *J Dermatol Treat* 2022;**33**:3104−18.
6. Mahmood T, Zaghi D, Menter A. Emerging oral drugs for psoriasis. *Expet Opin Emerg Drugs* 2015;**20**:209−20.

7. Armstrong AW, Read C. Pathophysiology, clinical presentation, and treatment of psoriasis: a review. *JAMA* 2020;**323**:1945−60.
8. Reich K, Papp KA, Blauvelt A, Tyring SK, Sinclair R, Thaci D, et al. Tildrakizumab versus placebo or etanercept for chronic plaque psoriasis (reSURFACE 1 and reSURFACE 2): results from two randomised controlled, phase 3 trials. *Lancet* 2017;**390**:276−88.
9. Bruschi ML, da Silva JB, Rosseto HC. Photodynamic therapy of psoriasis using photosensitizers of vegetable origin. *Curr Pharm Des* 2019;**25**:2279−91.
10. Makuch S, Drozdz M, Makarec A, Ziolkowski P, Wozniak M. An update on photodynamic therapy of psoriasis-current strategies and nanotechnology as a future perspective. *Int J Mol Sci* 2022;**23**:9845.
11. Zhu P, Wu ZJ, Yang ZL, Tang TT, Liao YH, Zhao W, et al. Aggregation-induced emission-active photosensitizer-mediated photodynamic therapy for anti-psoriasis. *Research* 2024;**7**:344.
12. Lin RK, Venkatesan P, Yeh CH, Chien CM, Lin TS, Lin CC, et al. Effective topical treatments using innovative NNO-tridentate vanadium(IV) complexes-mediated photodynamic therapy in a psoriasis-like mouse model. *J Mater Chem B* 2022;**10**:4759−70.
13. Wang H, Su DD, Huang RF, Shu F, Cheng F, Zheng G. Cellular nanovesicles with bioorthogonal targeting enhance photodynamic/photothermal therapy in psoriasis. *Acta Biomater* 2021;**134**:674−85.
14. Correia JH, Rodrigues JA, Pimenta S, Dong T, Yang ZC. Photodynamic therapy review: principles, photosensitizers, applications, and future directions. *Pharmaceutics* 2021;**13**:1332.
15. Cui SD, Guo XR, Wang S, Wei Z, Huang DL, Zhang XZ, et al. Singlet oxygen in photodynamic therapy. *Pharmaceuticals (Basel)* 2024;**17**:1274.
16. Nirmal GR, Liao CC, Lin ZC, Alshetaili A, Hwang E, Yang SC, et al. Topically applied pH-responsive nanogels for alkyl radical-based therapy against psoriasiform hyperplasia. *Drug Deliv* 2023;**30**:2245169.
17. Li LS, Lu JY, Liu J, Wu JC, Zhang XY, Meng Y, et al. Immune cells in the epithelial immune microenvironment of psoriasis: emerging therapeutic targets. *Front Immunol* 2024;**14**:1340677.
18. Ramadon D, McCrudden MTC, Courtenay AJ, Donnelly RF. Enhancement strategies for transdermal drug delivery systems: current trends and applications. *Drug Deliv Transl Res* 2022;**12**:758−91.
19. Kim YC, Park JH, Prausnitz MR. Microneedles for drug and vaccine delivery. *Adv Drug Deliv Rev* 2012;**64**:1547−68.
20. He J, Zhang Y, Yu X, Xu C. Wearable patches for transdermal drug delivery. *Acta Pharm Sin B* 2023;**13**:2298−309.
21. Zhi Chen B, Ting He Y, Qiang Zhao Z, Hao Feng Y, Liang L, Peng J, et al. Strategies to develop polymeric microneedles for controlled drug release. *Adv Drug Deliv Rev* 2023:115109.
22. Zhang Y, Yu J, Kahkoska AR, Wang J, Buse JB, Gu Z. Advances in transdermal insulin delivery. *Adv Drug Deliv Rev* 2019;**139**:51−70.
23. McAlister E, Kirkby M, Dominguez-Robles J, Paredes AJ, Anjani QK, Moffatt K, et al. The role of microneedle arrays in drug delivery and patient monitoring to prevent diabetes induced fibrosis. *Adv Drug Deliv Rev* 2021;**175**:113825.
24. Zeng Y, Wang C, Lei J, Jiang X, Lei K, Jin Y, et al. Spatiotemporally responsive cascade bilayer microneedles integrating local glucose depletion and sustained nitric oxide release for accelerated diabetic wound healing. *Acta Pharm Sin B* 2024;**14**:5037−52.
25. Yin M, Wu J, Deng M, Wang P, Ji G, Wang M, et al. Multifunctional magnesium organic framework-based microneedle patch for accelerating diabetic wound healing. *ACS Nano* 2021;**15**:17842−53.
26. Zhang X, Gan J, Fan L, Luo Z, Zhao Y. Bioinspired adaptable indwelling microneedles for treatment of diabetic ulcers. *Adv Mater* 2023;**35**:e2210903.
27. Yuan A, Xia F, Bian Q, Wu H, Gu Y, Wang T, et al. Ceria nanozyme-integrated microneedles reshape the perifollicular microenvironment for androgenetic alopecia treatment. *ACS Nano* 2021;**15**:13759−69.
28. Yin M, Zeng Y, Liu HQ, Zhang W, Wang C, Chen C, et al. Dissolving microneedle patch integrated with microspheres for long-acting hair regrowth therapy. *ACS Appl Mater Interfaces* 2023;**15**:17532−42.
29. Wang C, He G, Zhao H, Lu Y, Jiang P, Li W. Enhancing deep-seated melanoma therapy through wearable self-powered microneedle patch. *Adv Mater* 2024;**36**:e2311246.
30. Li X, Zhao Z, Zhang M, Ling G, Zhang P. Research progress of microneedles in the treatment of melanoma. *J Control Release* 2022;**348**:631−47.
31. Yang D, Chen M, Sun Y, Jin Y, Lu C, Pan X, et al. Microneedle-mediated transdermal drug delivery for treating diverse skin diseases. *Acta Biomater* 2021;**121**:119−33.
32. Zhang W, Chen Y, Zhao Z, Zheng H, Wang S, Liao Z, et al. Adoptive T(reg) therapy with metabolic intervention *via* perforated microneedles ameliorates psoriasis syndrome. *Sci Adv* 2023;**9**:eadg6007.
33. Bi DH, Qu F, Xiao WY, Wu JX, Liu P, Du HY, et al. Reactive oxygen species-responsive gel-based microneedle patches for prolonged and intelligent psoriasis management. *ACS Nano* 2023;**17**:4346−57.
34. Zeng Y, Wu L, Jiang X, Hu Y, Jin Y, Hu H, et al. Self-assembled hyaluronic acid nanoparticles delivered by polymeric microneedles for targeted and long-acting therapy of psoriasis. *Int J Pharm* 2025;**669**:125073.
35. Li W, Li S, Fan X, Prausnitz MR. Microneedle patch designs to increase dose administered to human subjects. *J Control Release* 2021;**339**:350−60.
36. Wu C, Yang X, Yang K, Yu Q, Huang C, Li F, et al. Compensatory effect-based oxidative stress management microneedle for psoriasis treatment. *Bioact Mater* 2025;**46**:229−41.
37. Kim JD, Kim M, Yang H, Lee K, Jung H. Droplet-born air blowing: novel dissolving microneedle fabrication. *J Control Release* 2013;**170**:430−6.
38. Wang H, Fu YX, Liu P, Qu F, Du S, Li Y, et al. Supramolecular dissolving microneedle patch loading hydrophobic glucocorticoid for effective psoriasis treatment. *ACS Appl Mater Interfaces* 2023;**15**:15162−71.